**TECHNICAL ARTICLE**

# Modeling Strain Localization in Microtextured Regions in a Titanium Alloy: Ti–6Al–4V

Kartik Kapoor[1] · Ryan Noraas[2] · Venkat Seetharaman[2] · Michael D. Sangid[1]

## Abstract

Large and highly textured regions, referred to as macrozones or microtextured regions, with sizes up to several orders of magnitude larger than those of the individual grains, are found in dual-phase titanium alloys as a consequence of the manufacturing process route. These macrozones have been shown to play a critical role in the failure of titanium alloys, specifically being linked to crack initiation and propagation during cyclic loading. Modeling microstructures containing macrozones using continuum-level formulations to describe the elastic–plastic deformation at the grain scale, i.e., crystal plasticity, poses computational challenges due to the large size of the macrozones, which in turn prevents the use of modeling approaches to understand their deformation behavior. In this work, a crystal plasticity-based modeling approach is implemented to model macrozones in Ti–6Al–4V. Further, to overcome the large computational expense associated with modeling microstructures containing macrozones, a modeling strategy is introduced based on a crystal plasticity description for the macrozone with a reduced-order model for the surrounding aggregate combining anisotropic elasticity and J2 plasticity, based on crystal plasticity-based training data. This modeling approach provides a grain-level description of deformation within macrozones using elastic–plastic continuum simulations, which has often been overlooked. Finally, the reduced-order model is used to investigate the strain localization within the microstructure and the effect of varying the misorientation tolerance on the localization of plastic strain within the macrozones.

**Keywords** Macrozones · Microtextured regions · Crystal plasticity · Reduced-order modeling · Misorientation threshold

## Introduction

Macrozones are unique crystallographic features that exist in titanium alloys. These features, which are highly textured, can have sizes up to 100 times larger the average grain size and may be seen as a region characterized by a single orientation via X-ray diffraction (XRD) [1]. The presence of macrozones in a given alloy is dependent on the processing route used to manufacture the alloy. Some authors propose that the collection of similarly orientated α-grains, which form macrozones, may originate from a common prior β-grain [1, 2]. Macrozones, also referred as microtextured regions (MTRs), play a key role in influencing the mechanical properties of

the material and are also known to be preferred sites for strain accumulation and crack initiation [1, 3–5], which makes their presence in the material critical for predicting damage and estimating fatigue life. However, due to the multiple length scales involved in the problem, with macrozones being ~ 100 times bigger than the individual grains, including macrozones in grain-scale damage models presents an issue that needs new strategies to address.

Macrozones have been characterized and studied using a number of experimental techniques, primarily electron backscatter diffraction (EBSD), scanning electron microscopy (SEM), and XRD. Le Biavant et al. [1] studied Ti–6Al–4V, with a bimodal microstructure using optical microscopy and SEM imaging to understand the microstructure along with XRD to carry out crystallographic texture analysis. Their analysis reveals that numerous small fatigue cracks form in macrozones which are favorable for prism and basal slip. Humbert et al. [6] analyzed the microstructure of IMI 834, a Ti alloy with a bimodal microstructure, and observed macrozones with sharp texture. They studied the possible

✉ Michael D. Sangid
  msangid@purdue.edu

1 School of Aeronautics and Astronautics, Purdue University, West Lafayette, IN 47907, USA

2 Materials and Process Engineering, Pratt & Whitney, East Hartford, CT 06118, USA

variant selection during the β to α transformation, which is influenced by the stored elasticity state, and as such, the variant selection follows the minimization of the elastic strain energy. However, Semiatin et al. [7] studied the effect of process variables on preferential variant selection following β-annealing and found no relation between variant selection and minimization of the strain energy. Uta et al. [3] carried out EBSD characterization to understand the orientation distribution and the crystallography of fracture surfaces in IMI 834 subject to dwell fatigue. They observe crack nucleation and propagation in macrozones with mostly primary α-grains having their c axes between 10° and 30° from the loading axis, which may be attributed to high stresses in these macrozones, resulting from low amount of plasticity due to difficulty in activation of basal and prismatic slip. Similar to Uta et al. [3], Bridier et al. [4] used EBSD to characterize the microstructure of Ti–6Al–4V, especially the sites for crack initiation during fatigue loading. They observed that fatigue crack formation takes place in macrozones which have their [0 0 0 1] axis aligned with the loading axis and suggested that, though crack formation takes place on the basal plane of the α-grain, the deformation of macrozones at the mesoscopic scale also plays an important role. Bantounas et al. [5] studied the dependence of c-axis orientation of the macrozone on crack initiation and observed that macrozones with their c-axis close to the loading direction were responsible for faceted fracture and the macrozones with their c-axis being perpendicular to the loading direction act as barriers to faceted crack growth. Echlin et al. [8] carried out high resolution (HR-DIC) on Ti–6Al–4V loaded in situ and observed strain localization in macrozones well below the macroscopic yield. In cyclic loading, they observe early activation of basal slip, which is localized, and further loading leads to prismatic and pyramidal (either $<a>$ or $<c+a>$) slip across multiple grains within favorably oriented macrozones. Bandyopadhyay et al. [9] carried out HR-DIC experiments on Ti–6Al–4V with MTRs to study the grain-level strain localization and accompanied it with crystal plasticity simulations to study the effect of high R ratios on MTRs. As with Echlin et al. [8], they also observe activation of multiple families of slip systems, even first-order pyramidal, particularly along $<c+a>$ directions in MTRs with their c-axis nearly parallel to the loading direction leading to the anomalous mean stress behavior on the high-cycle fatigue performance experienced by Ti–6Al–4V. Based on these observations, it is important to incorporate pyramidal slip systems into the crystal plasticity framework that deals with macrozones. In another HR-DIC study, Book et al. [10] investigated strain localization in additively manufactured Ti–6Al–4V and observed prior β-boundaries impede strain transmission, resulting in strain localization. Finally, Britton et al. [11] observed a higher geometrically necessary dislocation (GND) content (approximately twice) in macrozones as compared to the non-macrozone region in Ti–6Al–4V by calculating the intra-granular misorientation using EBSD. The higher GND density indicates that the macrozone may be susceptible to strain localization and hence crack initiation. All of the above reviewed literature suggests that macrozones play a crucial role in strain localization and crack initiation within dual-phase titanium alloys, and in a number of these studies, hard–soft MTR combinations are seen to be critical locations.

In order to understand the deformation mechanisms in a wide range of titanium alloys, specifically at the length scale of grains, a number of crystal plasticity models have been developed [9, 12–23] and used to model a number of alloys. Though none of these models has specifically been used to model macrozones, as the authors in these papers limit their simulations to smaller volumes due to the scope of their work as well as due to the computational time associated with modeling macrozones, there is nothing inherently missing in these models that prevents their application to model macrozones. Modeling macrozones using continuum-level formulations involving grain-level deformation is a challenging problem due to the size of the macrozones being orders of magnitude bigger than that of the individual grains. With grains being modeled using hundreds of elements, a single macrozone containing ~ 1000 grains will contain a minimum of 0.1 million elements within a single macrozone. Though meshing strategies using a coarser mesh may reduce the number of elements, the scale of simulation still remains large. With increasing computing power, it is possible to simulate microstructures with macrozones, albeit such simulations still take enormous computational resources and time to run. This limits the application of crystal plasticity-based approaches to model macrozones and paves the way for a reduced-order model that does not require such high demands for computational time.

Currently, the means of identifying macrozones within a microstructure is based on the value of the misorientation tolerance (specifically the misorientation angle) used to segment them, which may vary depending on the study in consideration. The process often involves visually identifying macrozones by selecting a region with similar orientations on an EBSD map. Based on the literature, the misorientation tolerance used to identify MTRs varies from 15° [24] to 20° [25–27]. In this work, a 20° misorientation tolerance is used initially to identify macrozones. Using a 20° misorientation tolerance, there is still an outstanding question that needs to be answered: Can the deformation within a macrozone be captured by treating the MTR as a single crystal or do the small misorientations within the macrozone play a role in strain localization and hence crack nucleation? In addition, by studying the heterogeneity in the strain accumulation, more insights about deformation within a macrozone can be attained.

**Fig. 1** Inverse pole figure (IPF) from EBSD on the region probed with a few macrozones highlighted using a 20° misorientation tolerance with the orientation of the c-axis displayed
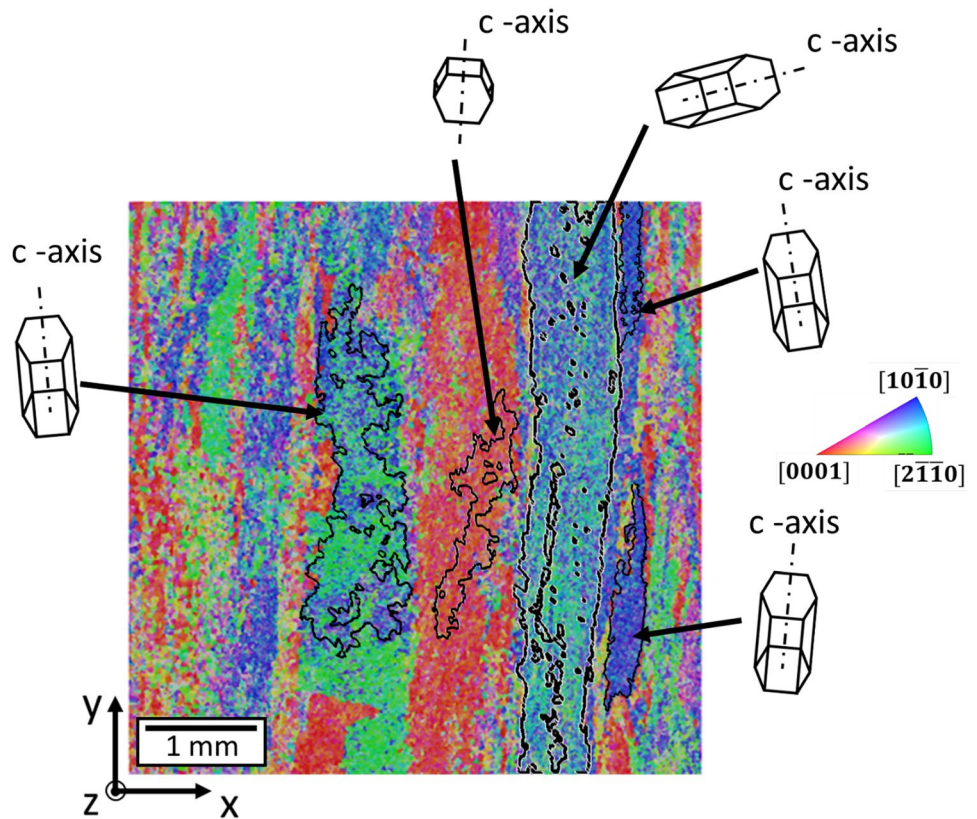
In this work, a CPFE-based modeling approach is used to model microstructures containing macrozones in a titanium alloy, Ti–6Al–4V. This is followed by developing a computationally efficient reduced-order modeling strategy for these microstructures with macrozones to overcome the computational challenges associated with their large size. This is achieved by modeling the large macrozones using crystal plasticity and the remaining microstructure using anisotropic elasticity coupled with J2 plasticity. Further, a unique way to determine the plasticity parameters for the reduced-order model, by relating texture to the plasticity parameters, is developed. The reduced-order model is then used to understand the effect of the misorientation tolerance used for identification of the macrozones on the deformation characteristics of the microstructure, specifically plastic strain localization within the macrozones. Additionally, the strain localization within the microstructure and its link to the orientations of the macrozones are also investigated.

## Material and EBSD Characterization

A number of experimental studies that deal with characterization of macrozones have been discussed in the previous section [1, 3–5, 8, 11], which go over the process of identifying macrozones using experimental data. In addition, Venkatesh et al. [28] present a detailed discussion to identify MTRs using a misorientation tolerance for the c-axis. With the primary focus of this paper being modeling macrozones, the experimental characterization is discussed in brief. The sample used for this study is cut from a longitudinal billet of Ti–6Al–4V to ensure it has MTRs. The sample containing macrozones is characterized using EBSD to determine the grain sizes, grain morphologies, and crystallographic orientations. It should be noted that only the HCP (α) phase is characterized, due to the length scale in consideration, which prevents the characterization of the BCC (β) phase with a significantly smaller size compared to the α-grains and being order of magnitudes smaller than the macrozones. Figure 1 shows the inverse pole figure (IPF) map obtained from the EBSD scan with an identified macrozone using a misorientation tolerance of 20°. The orientations of the EBSD points within the 20° misorientation tolerance are then averaged and assigned to the identified grain.

## Crystal Plasticity Model and FE Mesh Generation

The CPFE model used in this work is a phenomenological rate-dependent model implemented in Abaqus via the user material subroutine. For the benefit of the reader, the operators

used in the equations discussed in this paper are defined here. The tensor dot product between two second-order tensors is defined by the operator (·) and the multiplication between a scalar and a tensor or a scalar, and a scalar is represented with (*). The kinematics are captured by the multiplicative decomposition of the deformation gradient as follows:

$$F = F^e \cdot F^p \tag{1}$$

where $F$ is the total deformation gradient and $F^e$ and $F^p$ are the elastic and plastic parts, respectively. The plastic velocity gradient in the intermediate configuration is determined using the following equation:

$$L^P = \dot{F}^p \cdot (F^p)^{-1} = \sum_{i=1}^{N_{sys}} \dot{\gamma}^i \left( s_0^i \otimes n_0^i \right) \tag{2}$$

where $s_0^i$, $n_0^i$, and $\dot{\gamma}^i$ are the slip plane direction, slip plane normal, and the shearing rate for the $i$th slip system, respectively. The flow rule in this model is represented by a power law [29] as follows:

$$\dot{\gamma}^i = \dot{\gamma}_0 \left\langle \frac{|\tau^i - \chi^i| - K^i}{D^i} \right\rangle^m \operatorname{sgn}(\tau^i - \chi^i) \tag{3}$$

$\langle \rangle$ denotes Macaulay brackets with $\langle x \rangle = x$ for $x \geq 0$ and $\langle x \rangle = 0$ for $x < 0$. $\tau^i$, $D^i$, $\chi^i$, and $K^i$ are the resolved shear stress, slip system resistance, backstress, and the threshold stress for the $i$th slip system, respectively. $\dot{\gamma}_0$ and $m$ are the reference shearing rate and strain rate sensitivity, respectively, kept constant for all the slip systems. The threshold stress is further broken down into an evolving and a non-evolving component.

$$K^i = \frac{K_y^i}{\sqrt{d_{avg}}} + K_s^i \tag{4}$$

$K_y^i$ is a non-evolving constant, and $d_{avg}$ is the average grain size, which is similar in formation to the Hall–Petch relation [30, 31]. $K_s^i$ evolves according to the following equation:

$$\dot{K}_s^i = -\lambda K_s^i |\dot{\gamma}^i| \tag{5}$$

The slip system resistance evolves according to the following equation:

$$\dot{D}^i = H \sum_{j=1}^{N} q^{ij} |\dot{\gamma}^j| - H_D D^i \sum_{j=1}^{N} |\dot{\gamma}^j| \tag{6}$$

The backstress evolves according to the following equation:

$$\dot{\chi}^i = A \sum_{i=1}^{N_{sys}} \dot{\gamma}^i - A_D \chi^i \sum_{i=1}^{N_{sys}} |\dot{\gamma}^i| \tag{7}$$

**Table 1** Crystal plasticity parameters utilized in the simulations

| Parameter | Value |
|---|---|
| $\dot{\gamma}_0$ | 0.001 |
| $m$ | 15 |
| CRSS (MPa) | |
| Basal | 420 |
| Prism | 370 |
| Pyramidal-1 | 490 |
| Pyramidal-2 | 590 |
| $D$ (MPa) | |
| Basal | 148 |
| Prism | 98 |
| Pyramidal-1 | 218 |
| Pyramidal-2 | 318 |
| $d_{avg}$ (μm) | 19.8 |
| $K_y$ (MPa* $\sqrt{\mu m}$) | |
| Basal | 522.62 |
| Prism | 538.28 |
| Pyramidal-1 | 521.68 |
| Pyramidal-2 | 720.76 |
| $K_s$ (MPa) | |
| Basal | 147.06 |
| Prism | 144.18 |
| Pyramidal-1 | 143.12 |
| Pyramidal-2 | 158.23 |
| $\lambda$ | 50 |
| $C_{11}$ (MPa) | 162,400 |
| $C_{12}$ (MPa) | 92,000 |
| $C_{44}$ (MPa) | 49,700 |
| $C_{13}$ (MPa) | 69,000 |
| $C_{33}$ (MPa) | 180,700 |

A total of 24 slip systems: 3 $(0001)\langle 11\bar{2}0 \rangle$ basal, 3 $\{10\bar{1}0\}\langle 11\bar{2}0 \rangle$ prismatic, 6 $\{10\bar{1}1\}\langle 11\bar{2}0 \rangle$ first-order pyramidal, and 12 $\{10\bar{1}1\}\langle 11\bar{2}3 \rangle$ second-order pyramidal have been included in this model. The elastic constants are based on the values used in [14]. All the CPFE parameters that cannot be obtained from the literature with a good degree of certainty are fit to experimental stress–strain curves. The fitting procedure involves using a genetic algorithm to fit the CPFE constants used in Eqs. 1–7 with the objective function being minimizing the error between the experimental and simulated stress–strain curves. The initial values for the parameters are obtained from [14] and [15]. More details about the fitting routine can be found in [32], and the final fitted parameters are given in Table 1.

This crystal plasticity model is used to run simulations for a subsection of the EBSD scan shown in Fig. 1. The EBSD scan in Fig. 1 is used as an input to DREAM.3D, an open-source data analysis tool, specifically geared toward 3D materials [33] to create a finite element (FE) mesh with hexahedron elements. Details about generating the FE mesh using DREAM.3D can be
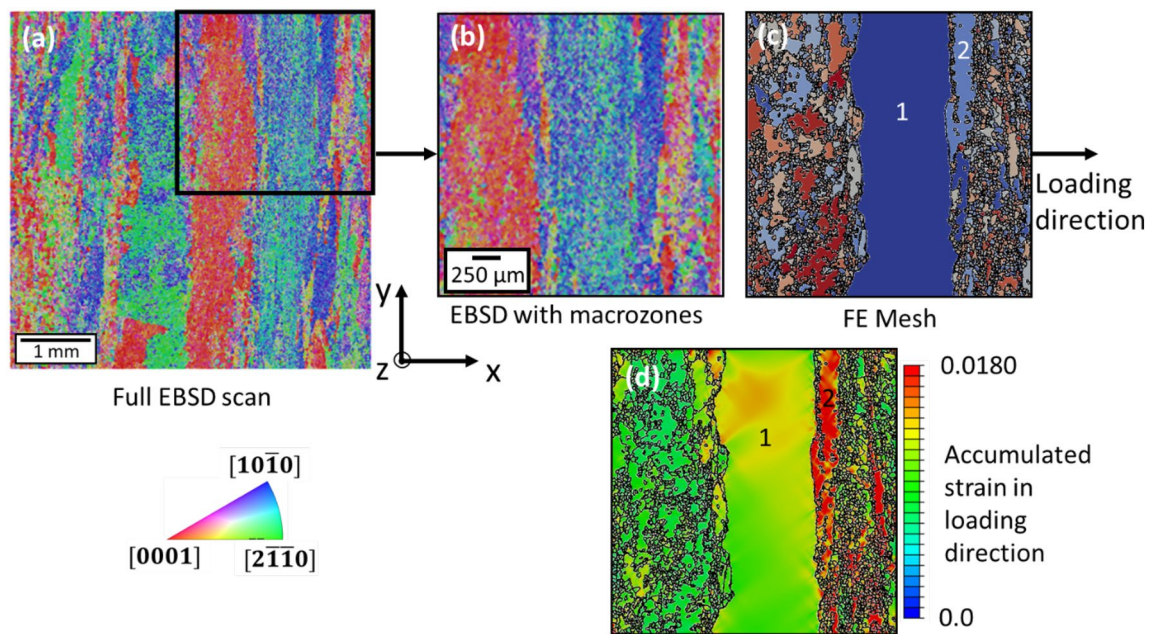
**Fig. 2** **a** Complete IPF map from the EBSD scan, **b** region of the EBSD map used for the simulations, **c** FE mesh of the region of interest (each grain colored differently for easy identification), generated from the EBSD scan using DREAM.3D with the two largest macrozones highlighted (1 and 2). **d** Total strain in the loading direction corresponding to a macroscopic strain of 1.2%. *Note*: The FE mesh is not 2D and has a thickness of two elements in the z (in-plane)- direction

found in [20]. This finite element mesh is then used as an input for the CPFE simulations as well as the reduced-order model simulations presented in the following sections. The area of the EBSD map that is simulated along with the FE mesh created and the result of the simulation (strain in the loading direction) are shown in Fig. 2. The FE mesh consists of 1,391,112 hexahedron elements, with an element size of 1 μm*1 μm*1 μm. The simulation takes 72 h to run using 320 processors.

## Reduced-Order Model

Running the full-scale CPFE simulations on the microstructures, like the one in Fig. 1, which are extremely large (on the order of millimeters), takes a long time (72 h for the current microstructure). Though simulations play an important role in understanding deformation in microstructures with macrozones, these large simulation times diminish their advantage and hence reduce the application of modeling approaches specifically in the industrial sector. To reduce the computational expense, and at the same time to understand the deformation behavior in and around the macrozones, a reduced-order model needs to be introduced. In order to capture the anisotropy that exists between grains due to their varying crystallographic orientations, it is essential that the elastic anisotropy is captured by rotating the elastic stiffness tensor according to the orientation of the grain with respect to the sample axis.

In the reduced-order plasticity model proposed and used in this work, the simulations for microstructures containing macrozones are run using a combined J2 plasticity and CPFE model. This involves using a full-scale CPFE formulation to model the large macrozones present (two in the current work) in the microstructure and using J2 plasticity with full anisotropic elasticity to model the remaining regions as shown in Fig. 3. It must be reiterated that the plasticity simulations are not elastically isotropic but do consider the crystallographic orientation of individual grains by rotating the anisotropic elastic constant tensor appropriately using Eq. 11, which can be seen in the variation in stress among different grains in Fig. 3.

The implementation of plasticity within Abaqus [34] is based on the elastic–plastic decomposition of the deformation gradient as in Eq. 1 but is simplified using a small strain assumption, which is valid for our simulations to give the additive strain rate decomposition.

$$\dot{\varepsilon} = \dot{\varepsilon}^{\mathrm{pl}} + \dot{\varepsilon}^{\mathrm{el}} \tag{8}$$

$\dot{\varepsilon}$ denotes the strain rate with superscripts "el" and "pl" representing the elastic and plastic parts, respectively. This equation can be written in its integral form over a time increment as follows:

$$\Delta\varepsilon = \Delta\varepsilon^{\mathrm{pl}} + \Delta\varepsilon^{\mathrm{el}} \tag{9}$$

The elastic behavior is modeled using Hooke's law:

$$\sigma = C^{\mathrm{grain}} \cdot \varepsilon^{\mathrm{el}} \tag{10}$$

**Fig. 3 a** FE mesh of the region of interest (each grain colored differently for easy identification). **b** CPFE-J2 plasticity simulations for microstructures with macrozones after 1.2% applied strain: Macrozones 1 and 2 modeled using crystal plasticity, and the remaining regions with anisotropic elasticity coupled with J2 plasticity
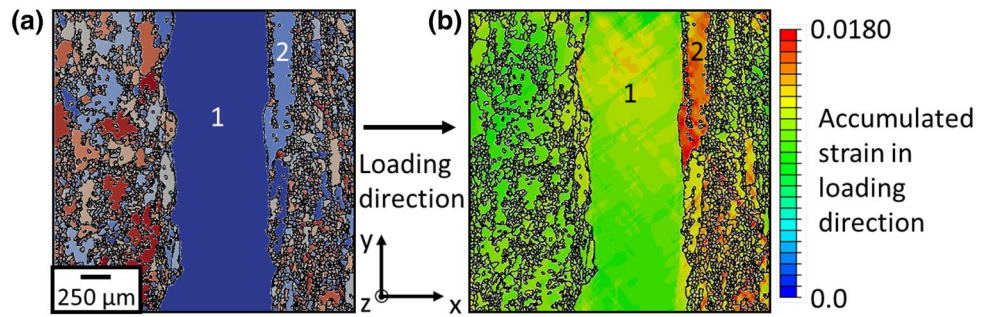


with

$$C^{\text{grain}} = D \cdot C \tag{11}$$

where $C^{\text{grain}}$ is the elastic constant tensor for the grain in consideration, $C$ is the single crystal elastic constant tensor, and $D$ is the rotation matrix constructed using the Euler angles of the grain in consideration. The plasticity model used in this work is a simple elastic–plastic model with the stress beyond the yield strain approximated using a straight line (linear isotropic hardening), as shown in Fig. 4, with the yield function, $f$, given by [35]:

$$f = \left( \bar{\sigma} - \sigma_Y \left( \bar{e}^{\text{pl}} \right) \right) = 0 \tag{12}$$

where $\bar{\sigma}$ is the equivalent deviatoric stress, $\sigma_Y \left( \bar{e}^{\text{pl}} \right)$ is the yield stress, and $\bar{e}^{\text{pl}}$ is the plastic part of the equivalent deviatoric strain $\bar{e}$ defined as follows:

$$\bar{e} = \sqrt{\frac{2}{3} e : e} \tag{13}$$

where

$$e = \varepsilon - I * \frac{1}{3} \text{trace}(\varepsilon) \tag{14}$$

where $\varepsilon$ is the strain tensor and $I$ is the identity tensor.

The equivalent deviatoric stress, $\bar{\sigma}$, is defined as follows:

$$\bar{\sigma} = \sqrt{\frac{3}{2} \sigma_D : \sigma_D} \tag{15}$$

with $\sigma_D$ being the deviatoric stress tensor.

$$\sigma_D = \sigma - I * \frac{1}{3} \text{trace}(\sigma) \tag{16}$$

where $\sigma$ and $I$ are the stress and identity tensor, respectively.

The yield stress, $\sigma_Y$, in the yield function given by Eq. 12 can be further broken down as follows [35]:

$$\sigma_Y = \sigma_{Y0} + \Omega \left( \bar{e}^{\text{pl}} \right) \tag{17}$$

with $\sigma_{Y0}$ being the yield stress at zero plastic strain ($\bar{e}^{\text{pl}} = 0$) and $\Omega \left( \bar{e}^{\text{pl}} \right)$ being the linear isotropic hardening function which can be defined as:

$$d\Omega \left( \bar{e}^{\text{pl}} \right) = h * d\bar{e}^{\text{pl}} \tag{18}$$
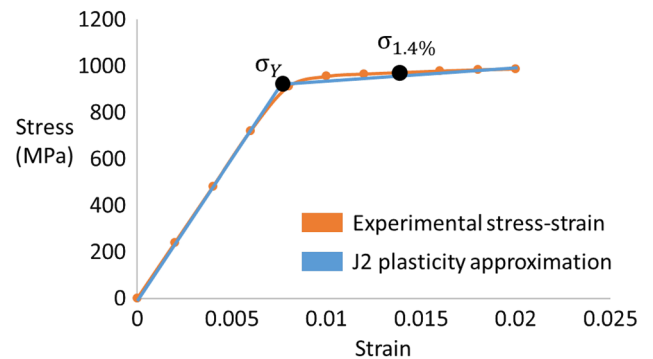


**Fig. 4** Approximation of the stress–strain curve used for determining J2 plasticity parameters with the two J2 plasticity parameters indicated in black

where $h$ is a constant and can be determined based on the data points from the stress–strain curve shown in Fig. 4. Equations 8 through 18 correspond to a continuum plasticity model with linear isotropic hardening. This model is available within the metal plasticity section of the Abaqus constitutive model database [34].

The CPFE framework used for the reduced-order model is the same as presented in "Crystal Plasticity Model and FE Mesh Generation" section, including the model parameters (Table 1). For the anisotropic elasticity, the elastic constants are the same as those of the CPFE model, since the elastic description of the material remains the same (Table 1). The additional parameters that are needed to run the elastic–plastic simulations are the stress at yield ($\sigma_Y$) and stress corresponding to a strain beyond yield, taken to be at 1.4% in this work ($\sigma_{1.4\%}$). Figure 4 shows the approximation of the stress–strain curve used for the J2 plasticity simulations along with its parameters.

The plasticity parameters needed for the simulations ($\sigma_Y$ and $\sigma_{1.4\%}$) can be determined from the stress–strain curves. One method of determining the stress–strain curves (and hence the parameters) is by performing tensile experiments and EBSD characterization on the microtensile samples with varying textures. However, since carrying out experimental tests on all the microstructures is time-consuming and may

Fig. 5 Procedure to create a Kearns factor database, which is used to determine the J2 plasticity parameters for a given microstructure
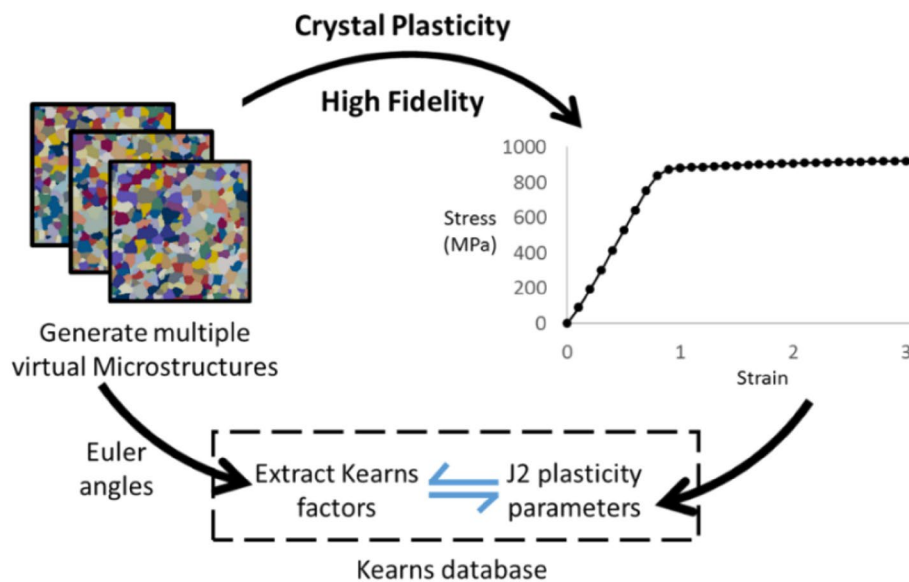


not always be feasible, a method to determine the plasticity parameters without using the experimental stress–strain curves is presented in the next section.

## Determining J2 Plasticity Parameters

To reduce the overall experimentation (and hence the associated time), a simpler and more feasible approach is utilized to train the reduced-order model, in which high fidelity full-scale CPFE modeling is leveraged to determine the parameters for the reduced-order J2 plasticity parameters. This is achieved by linking the microstructure, specifically the texture of the material to the stress–strain curve and hence to the J2 plasticity parameters. One such scalar quantity capable of quantifying texture for HCP materials is the Kearns factors [36], which are defined as follows:

$$f_j = \sum V_j \cos^2 (\alpha_j) \qquad (19)$$

where the Kearns factor, $f_j$, is the effective fraction of grains aligned with their [0001] axis, i.e., their c-axis parallel to the reference direction. $\alpha_j$ is the angle between the [0001] direction and the reference direction; $V_j$ is the volume fraction of grains with an angle between the [0001] direction and the reference direction being $\alpha_j$. To completely define texture in terms of the Kearns factors, three reference directions (mutually perpendicular) are needed, which are taken to be the laboratory frame in this work. This results in three orientation factors obeying the following relationship: $f_1 + f_2 + f_3 = 1$. Due to this relation between the three Kearns factors, only two out of the three factors are sufficient to describe the texture of a given pedigree of the material.

With the Kearns factors serving as a scalar representation of the texture of the material, the second step involves creating a link between these scalar factors and the plasticity parameters. This is achieved by creating a database relating the Kearns factors to the plasticity parameters. To populate the database, a large number of microstructures with randomly assigned orientations are used to run full-scale CPFE simulations. These microstructures are not complete 3D but are "2.5D" i.e., 2D with an extrusion for thickness of 4 elements, and consist of 360 grains meshed using 250,000 elements, which are sufficiently large to capture the required texture (but are not extremely large) and can be run in a matter of 4–5 h. These microstructures with randomly assigned orientations cover a large number of possible orientations out of the total possible orientations. The stress–strain curves obtained from these simulations can then be used to determine the J2 plasticity parameters and populate the database.

Using this database, given the microstructure of the material, the Kearns factors can be determined and linked to the corresponding J2 plasticity parameters. The process of creating the Kearns database is visually summarized in Fig. 5.

Since the Kearns factors follow the relation $f_1 + f_2 + f_3 = 1$, based on the chosen axes that are mutually perpendicular to each other, the texture of a given microstructure can be represented as a point on a unit cell of a Cartesian coordinate system with $f_1$, $f_2$ and $f_3$ being the mutually orthogonal axes. If the entire possible orientation space is considered, it will result in a plane with the equation $f_1 + f_2 + f_3 = 1$. To create the current database, nearly 1500 simulations with microstructures having varying orientations are run. The orientations corresponding to the microstructures that are simulated to populate the Kearns database are plotted in Fig. 6. The current database consists data from nearly 1500 simulations. In order to take
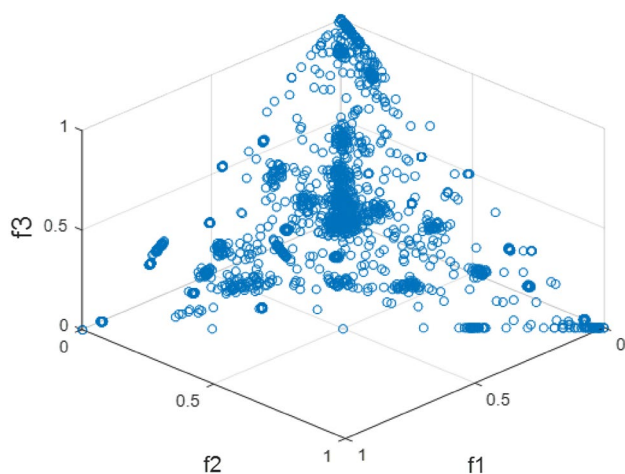
**Fig. 6** Orientations represented using the Kearns factors contained in the database plotted using the Kearns factors as the coordinate axes

into account the preferential textures that may exist in the real material with macrozones, a number of simulations carried out to generate the Kearns database are based on texture data obtained from actual samples of the material in consideration. It can be seen that a large portion of the orientation space is covered by the set of simulations conducted in this study. If a microstructure being simulated does not have its Kearns factors close to any of those plotted in Fig. 6, the J2 plasticity parameters are determined by interpolating between the available data points using the following equation:

$$\text{J2 parmeter (P)} = \frac{W_1 P_1 + W_2 P_2 + W_3 P_3}{W_1 + W_2 + W_3} \quad (20)$$

where $W_1$, $W_2$, and $W_3$ are the distances of the three closest points in the database, with distances being measured using the Kearns factors as the coordinate axis and $P_1$, $P_2$, and $P_3$ representing one of the J2 plasticity parameters of the closest points in the database, respectively. Both the parameters, $\sigma_Y$ and $\sigma_{1.4\%}$, are treated independently and can be obtained using Eq. 20.

## Validation

The reduced-order model, presented in "Crystal Plasticity Model and FE Mesh Generation" section, as well as the procedure developed to determine the plasticity parameters using the Kearns database, presented in "Determining J2 Plasticity Parameters" section, needs to be validated, in order to build confidence with the results obtained from the reduced-order model. A simple and reliable way to validate the precision of the reduced-order model is to compare the results with those of the full CPFE model. This is done by

carrying out two comparisons: One comparison is made at a macroscopic strain of 0.45%, where the microstructure is expected to be dominated by elastic strains to ensure the anisotropic elasticity captures the deformation below the yield point of the material, and the other comparison is made at 1.2% macroscopic strain, where the strain distribution is going to be a combination of elastic and plastic strain to validate the complete model. The comparisons are shown in Fig. 7.

From Fig. 7, it is seen that the strain distribution in the loading direction at a macroscopic strain of 0.45% is similar in both the full crystal plasticity and the reduced-order models, indicating that the anisotropic elasticity and microplasticity are captured appropriately. At 1.2% macroscopic strain, the strain map comparison, between the reduced-order (J2-CPFE) and full (CPFE) models, does not quantitatively relate to each other on a grain-by-grain basis, with the reduced-order model slightly under predicting the maximum strain values in macrozones 1 and 2. However, there is a good qualitative match in the regions of high and low strains within the microstructure, as seen in and near macrozones 1 and 2. The ability to capture hot spots in and around the macrozones is deemed the most important aspect of these models, which are correctly captured using the reduced-order model. In addition, the region of high strain in region labeled as "A", away from the macrozone, is captured in both the models. To further validate the model, the stress component in the loading direction is plotted in Fig. 8, and it is seen that the reduced-order model slightly under predicts the average stress values, but the stress localization is captured similarly in both the models. The qualitative match is significant as the reduced-order model takes nearly 1/5th the time to run on the same microstructural mesh. The reduction in time is important as running large CPFE models with appropriate size scales to capture the macrozones limits their widespread industrial use in damage modeling. In addition, the qualitative match ensures that if the model is used to predict the location of failure, the predicted location will be the same in the case of both the full-scale and the reduced-order models.

Next to validate the process of determining the J2 plasticity parameters from the Kearns database, the J2 plasticity parameters for a sample with a known experimental stress–strain curve are determined using the Kearns database discussed in "Determining J2 Plasticity Parameters" section. For the microstructure used to validate this process, the J2 plasticity parameters obtained from the experimental stress strain curve are: $\sigma_Y = 912$ MPa and $\sigma_{1.4\%} = 973$ MPa. From the Kearns database method, the parameters obtained are: $\sigma_Y = 906$ MPa and $\sigma_{1.4\%} = 1042$ MPa. The variation in values can be partially attributed to the stress–strain curves being obtained from macroscale experiments and the simulations corresponding to a smaller volume of the sample.

**Fig. 7** Total strain along the axial (loading) direction at **a** 0.45% strain (where the majority of strain is expected to be elastic) and **b** 1.2% (where the plastic strain is significant) with macrozones 1 and 2 identified
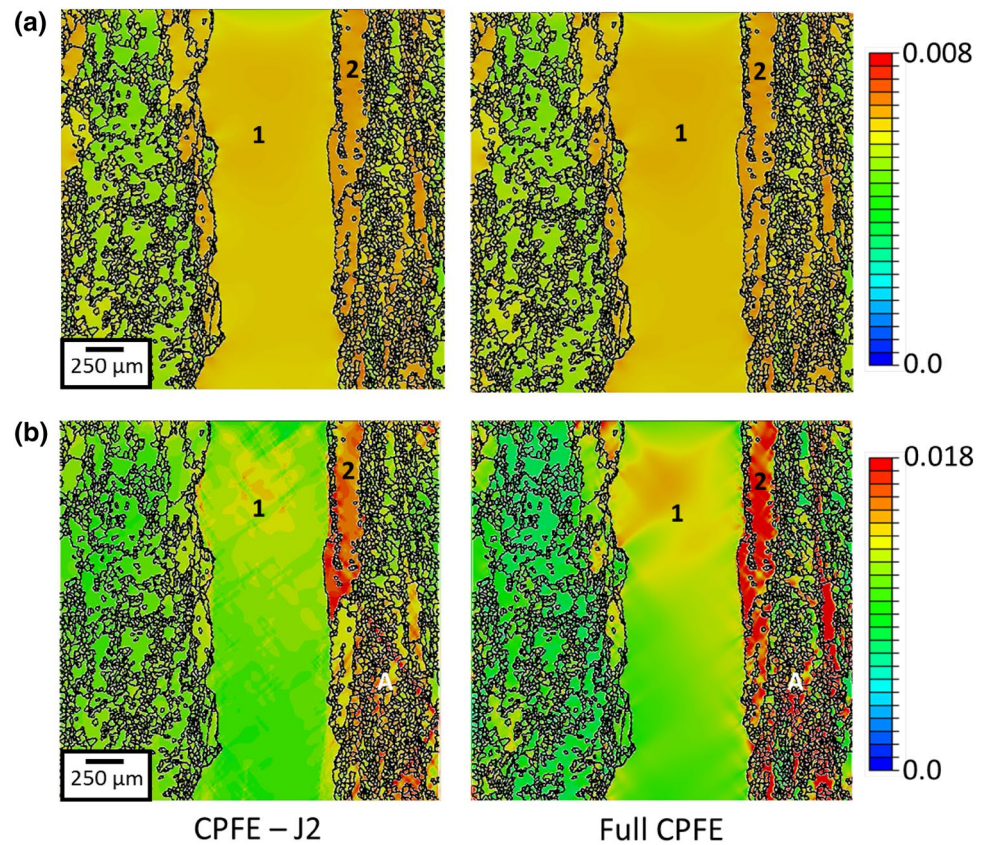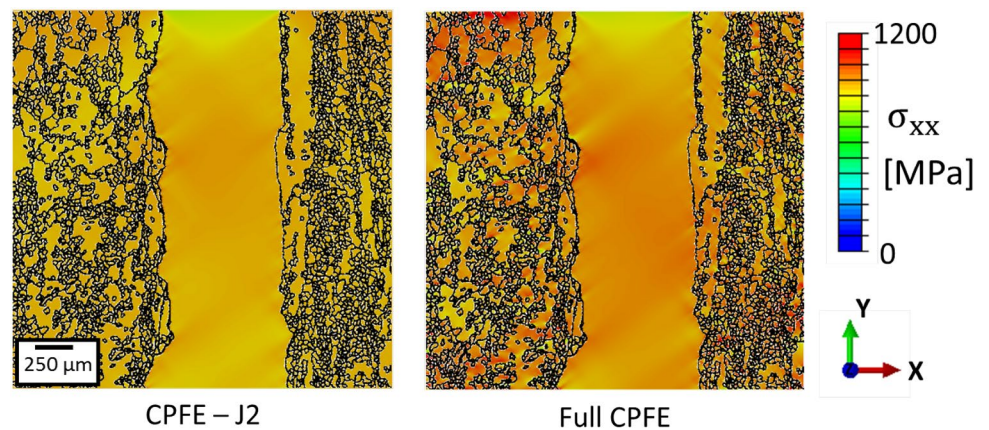


**Fig. 8** Stress distribution in the loading direction at 1.2% strain



## Effect of Misorientation Threshold on the Deformation in Macrozones

For the simulation discussed in the above sections, the macrozone within the microstructure being simulated is treated as a single grain, which is identified using a 20° misorientation tolerance between grains. The role of the misorientation tolerance used to identify macrozones is investigated in this section, specifically the effect of segmenting the macrozone using an 20°, 18°, 15°, 12°, 10°, 8°, and 5° misorientation

tolerance, i.e., to analyze the fidelity of the simulation by treating the macrozone as a single homogeneous grain. In each case, the misorientation tolerance within the macrozone is varied, while the region outside the macrozone is not altered and is still modeled using J2 plasticity with the same microstructure as studied in "Crystal Plasticity Model and FE Mesh Generation" section. To understand the effect of using different misorientation tolerances on the deformation within the macrozone, the plastic strain accumulation within the macrozone is plotted in Fig. 9. The plastic strain
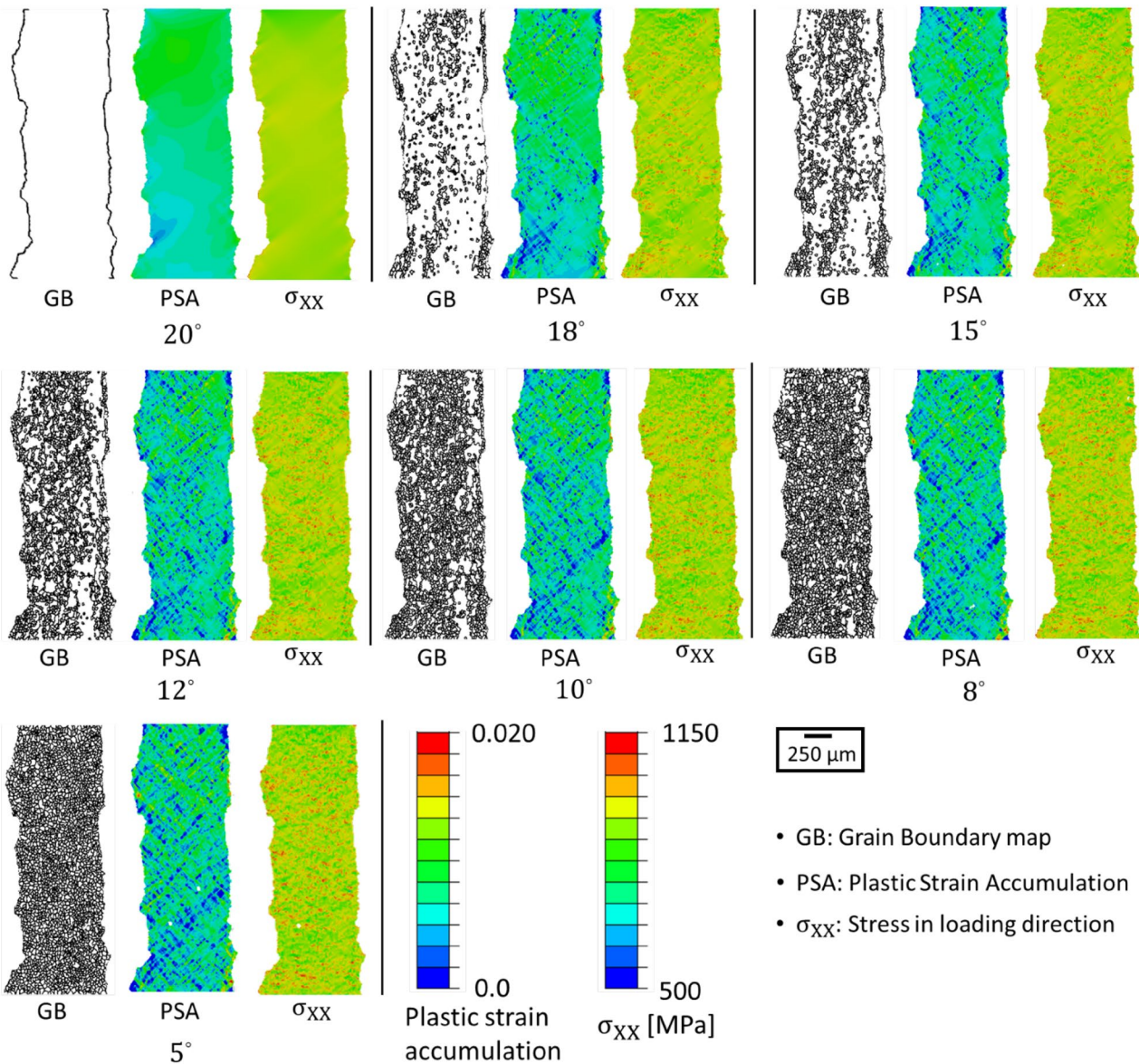
**Fig. 9** Variation in the plastic strain accumulation and the stress component in the loading direction within the largest macrozone with respect to the misorientation tolerance used to identify a macrozone

accumulation, a measure of plastic strain at a given material point, is defined as follows:

$$\dot{p} = \sqrt{\frac{2}{3}L_P : L_P}; \quad p = \int \dot{p}\,\mathrm{d}t \qquad (21)$$

From the plastic strain accumulation maps in Fig. 9, visually, a difference can be observed between modeling the macrozone as a single grain versus multiple grains; as with the increased number of grains, a higher degree of strain heterogeneity is observed within the macrozone. To quantify the strain heterogeneity within the macrozone and how it varies with the misorientation tolerance, a quantifiable

measure of strain heterogeneity, which measures the deviation of the strain within a grain from the average strain within the macrozone, is used:

$$\text{Hetrogeneity} = \sum_{k=1}^{N} \frac{(\varepsilon_k - \varepsilon_{\text{mean}})^2}{N} \qquad (22)$$

where $N$ is the number of grains within the macrozone and $\varepsilon_k$ and $\varepsilon_{\text{mean}}$ are the strain (in the loading direction) in the kth grain and the averaged strain in the macrozone, respectively. The value of heterogeneity, as it varies with the misorientation tolerance, is shown in Table 2. In addition, other parameters like the maximum, minimum, and the mean of

**Table 2** Measure of strain heterogeneity within the macrozone as a function of the misorientation tolerance

| Misorientation tolerance (no. of grains) | 20° (1 grain) | 18° (812 grains) | 15° (1316 grains) | 12° (1788 grains) | 10° (2381 grains) | 8° (2432 grains) | 5° (2617 grains) |
|---|---|---|---|---|---|---|---|
| Mean strain | 0.012 | 0.012 | 0.012 | 0.012 | 0.012 | 0.012 | 0.012 |
| Minimum value (grain averaged) | 0.012 | 0.070 | 0.070 | 0.069 | 0.070 | 0.069 | 0.069 |
| Maximum value (grain averaged) | 0.012 | 0.020 | 0.020 | 0.019 | 0.019 | 0.019 | 0.019 |
| Heterogeneity | 0.0 | 0.29 | 0.40 | 0.47 | 0.57 | 0.57 | 0.59 |

the plastic strain accumulation within the macrozone are also investigated.

By analyzing the effect of misorientation tolerance (and hence the number of grains) used to model a macrozone, from Table 2, it is seen that the heterogeneity increases with the decreasing misorientation tolerance (i.e., more grains); however, the increase from 10° to 5° is not significant as compared from 20° to 10°. There is a marked difference between modeling the macrozone as a single grain versus dividing it into multiple grains. However, the effect is not pronounced below a threshold of 10°. This suggests that a 10° misorientation tolerance is sufficient to capture the strain heterogeneity within the macrozones. The conventional threshold tolerance used for grains for a CPFE simulation varies from 2 to 5°. Based on the results of this study, using a threshold of 10° serves the purpose of capturing the strain heterogeneity and using this higher tolerance (as opposed to 2° or 5°) will reduce the simulation time due to the reduction in the number of grains. On the other hand, the conventional tolerance used during characterization to visually identify macrozones is 20°, as discussed in "Introduction" section. Thus, using a threshold of 10° (as opposed to the conventional 20°) will result in a conservative estimate of the size of the macrozone and result in visually smaller macrozones. An engineering trade-off exists between capturing the heterogeneity and gradients in the micromechanical fields within a macrozone, which necessitates a 10° misorientation threshold, and identifying the size of a macrozone associated with the characteristic length scale of damage, in which a 20° misorientation threshold is more appropriate.

## Investigating Strain Localization in the Microstructure

Since strain localization is known to be a precursor to failure [37, 38] and provides a good metric to predict damage, we investigate the strain distribution and localization within the microstructure. The strain distribution, along with the c-axis orientation of the two large macrozones, is shown in Fig. 10. It can be seen that high strain localization occurs in macrozone 2, which is adjacent to the other large macrozone (macrozone 1). To understand this strain distribution, the
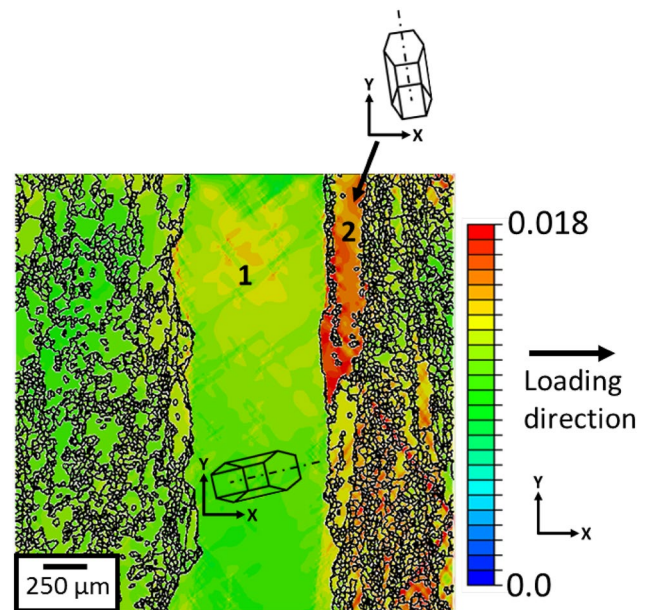


**Fig. 10** Strain distribution in the loading direction at 1.2% macroscopic strain (using the reduced-order model)

orientation of these macrozones is investigated. Macrozone 2 is well aligned for basal and prismatic slip, with its c-axis being nearly perpendicular to the loading direction (referred to as a soft grain), whereas, macrozone 1, having its c-axis relatively parallel to the loading direction (referred to as a hard grain), is not susceptible to basal and prismatic slip, which has a lower CRSS value compared to other slip systems [39]. This explains why strain localization is observed in macrozone 2 and not in macrozone 1.

In "Introduction" section, the reviewed literature suggested that macrozones play a key role in strain localization and crack nucleation. One of the most recently studied crack nucleation mechanisms in Ti alloys relates to the hard–soft grain combination which is also the region of high strain localization in the current microstructure. Multiple studies [40–42] suggest that hard–soft grain combinations lead to strain accumulation in the soft grain coupled with high stress concentration in the hard grain. The stress concentration in the hard grain then results in facet crack nucleation and hence failure. These effects are even more pronounced in

hard–soft macrozones than in hard–soft grains as the entire macrozone (which is orders of magnitude bigger than the individual grains) experiences high stress compared to the adjacent soft macrozone, resulting in higher possibility of facet crack nucleation. The simulation results presented in this paper using both the full-scale CPFE and the reduced-order models also result in high strain localization in the soft macrozone of the hard–soft macrozone combination. These results therefore suggest that the reduced-order model presented in this work can be incorporated into damage prediction frameworks.

## Conclusion

Deformation mechanisms and failure in dual-phase titanium alloys are based on multiple relevant length scales and therefore add complexity to the subsequent analysis. Macrozones play a major role in the strain localization and associated crack initiation. As a consequence, often titanium alloys are characterized to identify potential macrozones. But due to the multiple length scales, it presents challenges in microstructure-based modeling strategies. In this work, full-scale CPFE modeling is leveraged to develop a reduced-order model for macrozones in Ti–6Al–4V using a combination of J2 plasticity and CPFE modeling. To make the model versatile and usable for materials with varying textures, a unique way to determine the J2 plasticity parameters from texture information is developed, based on a set of Kearns factors. The results indicate that the reduced-order model provides promising results for the strain distribution in the sample, specifically within the macrozone. The reduction in time using the reduced-order model (from days to run a simulation to hours to run the same microstructural region) is substantial and hence paves the way for more widespread usage. Using this model, the choice of a misorientation tolerance used to identify a macrozone is investigated, and it is understood that modeling macrozone as a single grain does not capture the local strain heterogeneity, while using a misorientation tolerance of around 10° is sufficient to capture the local heterogeneity. Hard–soft macrozone combinations are well known to be potential sites for crack nucleation within these alloys. The results of these simulations also result in high strain localization in the soft macrozone of the hard–soft macrozone combination. This suggests that the simulation methodology, including the reduced-order model, can be integrated within damage models for the prediction of failure of titanium alloys.

## Compliance with Ethical Standards

**Conflict of interest** KK and MDS declare no conflicts of interests, while RN and VK are employees of Pratt & Whitney.

## References

1. Le Biavant K, Pommier S, Prioul C (2002) Local texture and fatigue crack initiation in a Ti–6Al–4V titanium alloy. Fatigue Fract Eng Mater Struct 25:527–545. https://doi.org/10.1046/j.1460-2695.2002.00480.x
2. Gey N, Bocher P, Uta E, Germain L, Humbert M (2012) Texture and microtexture variations in a near-α titanium forged disk of bimodal microstructure. Acta Mater 60:2647–2655. https://doi.org/10.1016/j.actamat.2012.01.031
3. Uta E, Gey N, Bocher P, Humbert M, Gilgert J (2009) Texture heterogeneities in αp/αs titanium forging analysed by EBSD-Relation to fatigue crack propagation. J Microsc 233:451–459. https://doi.org/10.1111/j.1365-2818.2009.03141.x
4. Bridier F, Villechaise P, Mendez J (2008) Slip and fatigue crack formation processes in an α/β titanium alloy in relation to crystallographic texture on different scales. Acta Mater 56:3951–3962. https://doi.org/10.1016/j.actamat.2008.04.036
5. Bantounas I, Dye D, Lindley TC (2010) The role of microtexture on the faceted fracture morphology in Ti–6Al–4V subjected to high-cycle fatigue. Acta Mater 58:3908–3918. https://doi.org/10.1016/j.actamat.2010.03.036
6. Humbert M, Germain L, Gey N, Bocher P, Jahazi M (2006) Study of the variant selection in sharp textured regions of bimodal IMI 834 billet. Mater Sci Eng A 430:157–164. https://doi.org/10.1016/j.msea.2006.05.047
7. Semiatin SL, Kinsel KT, Pilchak AL, Sargent GA (2013) Effect of process variables on transformation-texture development in Ti–6Al–4V sheet following beta heat treatment. Metall Mater Trans A 44:3852–3865. https://doi.org/10.1007/s11661-013-1735-6
8. Echlin MP, Stinville JC, Miller VM, Lenthe WC, Pollock TM (2016) Incipient slip and long range plastic strain localization in microtextured Ti–6Al–4V titanium. Acta Mater 114:164–175. https://doi.org/10.1016/j.actamat.2016.04.057
9. Bandyopadhyay R, Mello AW, Kapoor K, Reinhold MP, Broderick TF, Sangid MD (2019) On the crack initiation and heterogeneous deformation of Ti–6Al–4V during high cycle fatigue at high R ratios. J Mech Phys Solids 129:61–82. https://doi.org/10.1016/j.jmps.2019.04.017
10. Book TA, Sangid MD (2016) Strain localization in Ti–6Al–4V Widmanstätten microstructures produced by additive manufacturing. Mater Charact 122:104–112. https://doi.org/10.1016/j.matchar.2016.10.018
11. Britton TB, Birosca S, Preuss M, Wilkinson AJ (2010) Electron backscatter diffraction study of dislocation content of a macrozone in hot-rolled Ti–6Al–4V alloy. Scr Mater 62:639–642. https://doi.org/10.1016/j.scriptamat.2010.01.010
12. Goh C-H, Neu RW, McDowell DL (2003) Crystallographic plasticity in fretting of Ti–6AL–4V. Int J Plast 19:1627–1650. https://doi.org/10.1016/S0749-6419(02)00039-6
13. Mayeur JR, McDowell DL (2007) A three-dimensional crystal plasticity model for duplex Ti–6Al–4V. Int J Plast 23:1457–1485. https://doi.org/10.1016/j.ijplas.2006.11.006
14. Zhang M, Zhang J, McDowell DL (2007) Microstructure-based crystal plasticity modeling of cyclic deformation of Ti–6Al–4V.

Int J Plast 23:1328–1348. https://doi.org/10.1016/j.ijplas.2006.11.009

15. Bridier F, McDowell DL, Villechaise P, Mendez J (2009) Crystal plasticity modeling of slip activity in Ti–6Al–4V under high cycle fatigue loading. Int J Plast 25:1066–1082. https://doi.org/10.1016/j.ijplas.2008.08.004

16. Hasija V, Ghosh S, Mills MJ, Joseph DS (2003) Deformation and creep modeling in polycrystalline Ti–6Al alloys. Acta Mater 51:4533–4549. https://doi.org/10.1016/S1359-6454(03)00289-1

17. Deka D, Joseph DS, Ghosh S, Mills MJ (2006) Crystal plasticity modeling of deformation and creep in polycrystalline Ti-6242. Metall Mater Trans A 37:1371–1388. https://doi.org/10.1007/s11661-006-0082-2

18. Dunne FPE, Rugg D, Walker A (2007) Lengthscale-dependent, elastically anisotropic, physically-based hcp crystal plasticity: application to cold-dwell fatigue in Ti alloys. Int J Plast 23:1061–1083. https://doi.org/10.1016/j.ijplas.2006.10.013

19. Kapoor K, Sangid MD (2018) Initializing type-2 residual stresses in crystal plasticity finite element simulations utilizing high-energy diffraction microscopy data. Mater Sci Eng A 729:53–63. https://doi.org/10.1016/j.msea.2018.05.031

20. Kapoor K, Yoo YSJ, Book TA, Kacher JP, Sangid MD (2018) Incorporating grain-level residual stresses and validating a crystal plasticity model of a two-phase Ti–6Al–4V alloy produced via additive manufacturing. J Mech Phys Solids 121:447–462. https://doi.org/10.1016/j.jmps.2018.07.025

21. Zhang Z, Jun T-S, Britton TB, Dunne FPE (2016) Determination of Ti-6242 α and β slip properties using micro-pillar test and computational crystal plasticity. J Mech Phys Solids 95:393–410. https://doi.org/10.1016/j.jmps.2016.06.007

22. Zheng Z, Balint DS, Dunne FPE (2016) Dwell fatigue in two Ti alloys: an integrated crystal plasticity and discrete dislocation study. J Mech Phys Solids 96:411–427. https://doi.org/10.1016/j.jmps.2016.08.008

23. Cuddihy MA, Stapleton A, Williams S, Dunne FPE (2017) On cold dwell facet fatigue in titanium alloy aero-engine components. Int J Fatigue 97:177–189. https://doi.org/10.1016/j.ijfatigue.2016.11.034

24. Salem AA, Shaffer JB, Kublik RA, Wuertemberger LA, Satko DP (2017) Microstructure-informed cloud computing for interoperability of materials databases and computational models: microtextured regions in Ti alloys. Integr Mater Manuf Innov 6:111–126. https://doi.org/10.1007/s40192-017-0090-7

25. Pilchak AL, Li J, Rokhlin SI (2014) Quantitative comparison of microtexture in near-alpha titanium measured by ultrasonic scattering and electron backscatter diffraction. Metall Mater Trans A 45:4679–4697. https://doi.org/10.1007/s11661-014-2367-1

26. Pilchak AL, Shank J, Tucker JC, Srivatsa S, Fagin PN, Semiatin SL (2016) A dataset for the development, verification, and validation of microstructure-sensitive process models for near-alpha titanium alloys. Integr Mater Manuf Innov 5:14. https://doi.org/10.1186/s40192-016-0056-1

27. Woodffield AP, Gorman MD, Corderman RR, Sutliff JA, Yamrom B (1995) Effect of microstructure on dwell fatigue behavior of Ti-6242, In: Titan.'95 Sci Technol

28. Venkatesh V, Tamirisa S, Sartkulvanich J, Calvert K, Dempster I, Saraf V, Salem AA, Rokhlin S, Broderick T, Glavicic MG, Morton T, Shankar R, Pilchak A (2016) Icme of microtexture evolution in dual phase titanium alloys. In: Proceedings of the 13th World Conference on Titanium. John Wiley & Sons, pp 1907–1912. https://doi.org/10.1002/9781119296126.ch319

29. Mayeur JR, McDowell DL, Neu RW (2008) Crystal plasticity simulations of fretting of Ti–6Al–4V in partial slip regime considering effects of texture. Comput Mater Sci 41:356–365. https://doi.org/10.1016/j.commatsci.2007.04.020

30. Hall EO (1951) The deformation and ageing of mild steel: III discussion of results. Proc Phys Soc Sect B. 64:747. https://doi.org/10.1088/0370-1301/64/9/303

31. Petch NJ (1953) The cleavage strength of polycrystals. J Iron Steel Inst 174:25–28. https://doi.org/10.1007/BF01972547

32. Bandyopadhyay R, Prithivirajan V, Sangid MD (2019) Uncertainty quantification in the mechanical response of crystal plasticity simulations. JOM. https://doi.org/10.1007/s11837-019-03551-3

33. Groeber MA, Jackson MA (2014) DREAM.3D: a digital representation environment for the analysis of microstructure in 3D. Integr Mater Manuf Innov 3:5. https://doi.org/10.1186/2193-9772-3-5

34. Abaqus Documentation (2017)

35. Dunne F, Petrinic N (2005) Introduction to computational plasticity. Oxford University Press, Oxford

36. Kearns JJ (1965) Thermal expansion and preferred orientation in Zircaloy (LWBR Development Programe)

37. Sangid MD (2013) The physics of fatigue crack initiation. Int J Fatigue 57:58–72. https://doi.org/10.1016/j.ijfatigue.2012.10.009

38. Antolovich SD, Armstrong RW (2014) Plastic strain localization in metals: origins and consequences. Prog Mater Sci 59:1–160. https://doi.org/10.1016/j.pmatsci.2013.06.001

39. Lütjering G, Williams JC (2007) Titanium. Springer, Berlin

40. Dunne FPE, Walker A, Rugg D (2007) A systematic study of hcp crystal orientation and morphology effects in polycrystal deformation and fatigue. Proc R Soc A Math Phys Eng Sci 463:1467–1489. https://doi.org/10.1098/rspa.2007.1833

41. Zhang K, Yang KV, Huang A, Wu X, Davies CHJ (2015) Fatigue crack initiation in as forged Ti–6Al–4V bars with macrozones present. Int J Fatigue 80:288–297. https://doi.org/10.1016/j.ijfatigue.2015.05.020

42. Zheng Z, Balint DS, Dunne FPE (2016) Discrete dislocation and crystal plasticity analyses of load shedding in polycrystalline titanium alloys. Int J Plast 87:15–31. https://doi.org/10.1016/j.ijplas.2016.08.009